An epigraphene platform for coherent 1D nanoelectronics

Vladimir Prudkovskiy, Yiran Hu, Kaimin Zhang, Yue Hu, Peixuan Ji, Grant Nunn, Jian Zhao, Chenqian Shi, Antonio Tejeda, Alessandro de Cecco, et al.

▶ **To cite this version:**

Vladimir Prudkovskiy, Yiran Hu, Kaimin Zhang, Yue Hu, Peixuan Ji, et al.. An epigraphene platform for coherent 1D nanoelectronics. 2019. hal-02350189

HAL Id: hal-02350189
https://hal.science/hal-02350189

Preprint submitted on 8 Nov 2019

HAL is a multi-disciplinary open access archive for the deposit and dissemination of scientific research documents, whether they are published or not. The documents may come from teaching and research institutions in France or abroad, or from public or private research centers.

L'archive ouverte pluridisciplinaire **HAL**, est destinée au dépôt et à la diffusion de documents scientifiques de niveau recherche, publiés ou non, émanant des établissements d'enseignement et de recherche français ou étrangers, des laboratoires publics ou privés.

An epigraphene platform for coherent 1D nanoelectronics

*Vladimir Prudkovskiy[1, 2, 3], Yiran Hu[2], Kaimin Zhang[1], Yue Hu[2], Peixuan Ji[1], Grant Nunn[2], Jian Zhao[1], Chenqian Shi[1], Antonio Tejeda[4, 5], Alessandro De Cecco[3], Clemens Winkelmann[3], Yuxuan Jiang[6], Tianhao Zhao[2], Zhigang Jiang[2], Lei Ma[1†], Claire Berger[3 ,2], Walt A. de Heer[1, 2 *]*

[1] Tianjin International Center of Nanoparticles and Nanosystems, Tianjin University, 92 Weijin Road, Nankai District, China
[2] Georgia Institute of Technology, School of Physics, Atlanta, Georgia 30332, United States
[3] Univ. Grenoble Alpes, CNRS, Grenoble INP, Institut Néel, 38000 Grenoble, France
[4] Laboratoire de Physique des Solides, CNRS, Univ. Paris-Sud, Université Paris-Saclay, Bât. 510, 91405 Orsay, France
[5] Synchrotron SOLEIL, L'Orme des Merisiers, Saint-Aubin, 91192 Gif sur Yvette, France
[6] National High Magnetic Field Laboratory, Tallahassee, Florida 32310, United States

* corresponding author : e-mail: walter.deheer@physics.gatech.edu
† corresponding author : e-mail: maleixinjiang@tju.edu.cn

Abstract

Exceptional edge state ballistic transport, first observed in graphene nanoribbons grown on the sidewalls of trenches etched in electronics grade silicon carbide even at room temperature, is shown here to manifest in micron scale epigraphene structures that are conventionally patterned on single crystal silicon carbide substrates. Electronic transport is dominated by a single electronic mode, in which electrons travel large distances without scattering, much like photons in an optical fiber. In addition, robust quantum coherence, non-local transport, and a ground state with half a conductance quantum are also observed. These properties are explained in terms of a ballistic edge state that is pinned at zero energy. The epigraphene platform allows interconnected nanostructures to be patterned, using standard microelectronics methods, to produce phase coherent 1D ballistic networks. This discovery is unique, providing the first feasible route to large scale quantum coherent graphene nanoelectronics, and a possible inroad towards quantum computing.

1. Epigraphene nanoelectronics

In 1909 the silicon carbide LED (light emitting diode), was demonstrated (see refs in [1]). At that time, the still widely used conducting graphene ink, AquaDAG, was also invented. It was made from the graphene layer that forms on silicon carbide crystals (SiC) when they are heated. In that process a graphene layer forms, whose honeycomb lattice is atomically aligned with the crystal lattice of the SiC. That is, the graphene layer is epitaxial[2]. This epigraphene layer had been intensely studied in the last century in the context of SiC electronics research[1], but its intrinsic electronics properties were not considered.

The fact that graphene itself could be a 2D electronic material was first recognized in 2001 by the Georgia Tech epigraphene group (GTEG)[3]. It was inspired by their earlier discovery of room temperature ballistic transport properties of carbon nanotubes[4] combined with the realization that the electronic structure of graphene ribbons[5,6] is remarkably similar to that of carbon nanotubes. In addition, high performance, high density nanoelectronics requires single crystal substrates and epitaxy[7], to ensure the essential nanoscale precision and reproducibility. By those criteria, epigraphene is the ideal, and in fact currently the only, viable choice for high performance graphene nanoelectronics.

The GTEG had produced the first epigraphene devices in 2002. By then, calculations[5,6] had predicted that, like the ground state of carbon nanotubes[4,8-10], the edge states in neutral graphene ribbons are 1D ballistic conductors. Later edge-state theory[11,12] predicted numerous additional important properties, further amplifying the potential of graphene edge state electronics.

In 2010 the GTEG produced epigraphene nanoribbons, by thermally annealing 20 nm deep trenches that were etched in the polar (0001) facet of hexagon silicon carbide (H-SiC)[13]. The narrow graphene ribbons grown on the sloping sidewalls of steps and trenches[13-16] were found to have nanotube-like 1D ballistic properties[4,17]. Subsequently, room-temperature edge state transport was reported with unprecedented mean free paths (mfp) λ>40 μm, about 1000 times larger than the mfp of the bulk graphene[14]. However, the sloping sidewall geometry is poorly suited for electronics. Subsequently, we correctly conjectured that that the sloping SiC sidewalls were essential. Accordingly, we developed the capability to cut and polish SiC wafers from bulk SiC rods along the directions dictated by the sloping sidewalls. The properties of graphene grown on those non-polar crystal faces exceeded our expectations.

We show here, that the edge states of conventionally patterned devices on non-polar planar SiC substrates have all of the 1D ballistic properties observed on sidewall graphene, including the exceptionally large mfp's, and transport involving a single conductance quantum[14]. In addition, an unexplained half conductance quantum state is observed, as well as Fabry-Perot resonances and non-local transport, that demonstrate quantum coherence. These features show that quantum coherent interconnected quasi-1D networks can be patterned using conventional lithographic methods, making this new material an ideal platform for quasi-1D quantum coherent nanoelectronics: the essentially unexplored next frontier of electronics, as epitomized in quantum computing.

2. Graphene edge states

According to tight-binding calculations[5,6,18] (Fig.1) the electronic structure of the edge state of a graphene ribbon with zigzag edges consists of a dispersionless, non-conducting band at energy E=0 (the flat band) localized at the ribbon edge, two ballistic linearly dispersing bands with the graphene Fermi velocity $|dE/dk|=c^*$ (k is the wave number) for $|E|>0$, and an evanescent region near E=0, with wavefunctions that decay going into the bulk, Fig. 1c. The flat band represents a large density of states exactly at E=0 and corresponds to about 4 states per nm at the edge. It is half-filled at the charge neutrality point (CNP or Dirac point)[5,6,11,19]. The ballistic edge state conductance was predicted to be $G=2G_0=2e^2/h$, where G_0 is the conductance quantum, e is the electronic charge and h is Planck's constant[18].

Akhmerov and Beenakker[20] showed that this tight-binding band structure generically applies to graphene ribbons with arbitrary edges (excluding perfect armchair edges). More elaborate recent theory (beyond tight-binding), comprehensively reviewed in ref[11], predicts that edges of graphene systems can host localized states with evanescent wave functions that have properties that are radically different from those of the Dirac electrons in bulk, including edge ferromagnetism[5,21,22], the quantum anomalous Hall and the quantum spin Hall phases, where transport involves topologically protected edge states[18,23]. This clearly greatly expands their potential for novel electronics.

A graphene ribbon has distinct modes or electronic subbands (Fig. 1c), analogous to modes of an optical fiber. The Landauer equation states that the conductance G in the ribbon (with length L and width W) is the sum of the subband conductances. In simplified form (at T=0K)[24]:

$$G = G_0 \sum_\nu \Theta_\nu \approx G_0 \sum_\nu^{occ} g_\nu (1 + L/\lambda_\nu)^{-1} \qquad (1)$$

where, Θ_ν is the transmission coefficient ($0 \le \Theta_\nu \le 1$), g_0=2 for ν=0 and g_ν=4 for $\nu \neq 0$, and λ_ν is the electronic mfp of the ν^{th} subband[24]. The sum is over the subbands that cross the Fermi level E_F and $E_F=\pm\hbar c^* k_F$ is the Fermi energy ($k_F = \sqrt{\pi n}$ is the Fermi wave vector).

In the diffusive limit, when $\lambda_\nu << L$, then $G = ne\mu W/L$ where n is the charge density and μ is the mobility. For graphene ribbons g_0=2 and $g_{\nu\neq 0}$=4. Congruently, for graphene sidewall ribbons we reported[14]:

$$G = G^{edge} + G^{bulk} = G_0 \left(1 + \frac{L}{\lambda_0}\right)^{-1} g_0(B,T) + ne\mu W/L \qquad (2)$$

G^{edge} is the (ballistic) conductance of the edges state (ν=0, λ_ν>10 μm) and G^{bulk} is the diffusive conductance of the bulk ($\nu \neq 0$, $\lambda_\nu \approx 20$ nm)[14], due to scattering from charges in the substrate[25,26] that is found to be essentially temperature independent. For sidewall ribbons at CNP, we showed that g_0=1 rather than 2 for temperatures 20K≤T≤300K[14]. These properties are again found here.

Sidewall ribbons are ballistic conductors at CNP (n=0) (Eq. 2).[14,16,27] In contrast, due to edge disorder, at low temperature ribbons produced from exfoliated graphene are insulators at CNP[28], even when BN substrates are used[29] on which the bulk graphene mobility is extremely large[30].

As expected (see, for example Ref.[24]) and observed[14], an invasive probe placed on a ballistic ribbon with resistance R_{Bal} doubles its resistance to $2R_{Bal}$ because the probe divides the ribbon into two independent ballistic segments. For multiple probes, the resistance increases by $1R_{Bal}$ for each probe[14]. Segmentation both demonstrates and quantifies ballistic transport[14]. While a segmented ballistic network, as described above, electrically mimics a conventional diffusive resistor network, the physics is quite different as is clear from Eqs. 1 and 2[24].

As demonstrated experimentally here, the half-filled flat band at CNP pins the Fermi level at E=0 at the ribbon edge[31,32]. The charge induced on the graphene by the gate, is depleted near the edge[32,33] and absorbed in the flat band. The resulting electrostatic fields cause band bending (Fig. 1 b) and the potential $U(x)$ (measured from E_F to CNP) a distance x from the edge is approximately

$$U(x) \approx U_o\left(1 - e^{-x/d}\right)$$
$$n(x) \approx n_o\left(1 - e^{-x/d}\right)^2 \qquad (3)$$

where U_0 and n_0 are the potential and charge density far from the edge, and d is the dielectric thickness[32]. Band bending near the edge confines the electronic waves in the direction transverse to the edge. The resulting guided 'fiber-optic' modes propagate along the crystal edge as plane waves and decaying into the bulk as evanescent waves (see Ref.[12] Fig. 1). For simplicity, we call the dispersing component of the edge state near E=0, the EVE (evanescent edge state), without subscribing to any specific theoretical model.

Since the EVE is pinned to E=0, its response to the gate voltage is suppressed so that $g_0(B,T,n) \approx g_0(B,T,n=0)$. Therefore, as shown here and previously in sidewall ribbons[14], the conductance of the EVE is in parallel with the bulk and independent of the gate voltage, consistent with Eq.2.

The large density of states at E=0 is a general property of polycyclic aromatic hydrocarbons with zigzag-like edge atoms[34-38] has been observed in STM studies[39-41]. Similarly a large local density of states and Fermi level pinning at E=0 was observed, and attributed to carbon vacancies[42] in C-face epigraphene multilayers[43]. In Si-face epigraphene, Fermi level pinning at E=0 by the buffer layer causes extended ν=2 quantum Hall plateaus[44]. The physics of pinning at E=0 in graphene is similar to mid-gap defect pinning in semiconductors.[31,32]

When the flat band is saturated (or depleted) by the gate induced charge density n, the edge state unpins, approximately when $|n| \approx 1/a_0 d \approx 4\ 10^{13}$ cm^{-2} for d =30 nm where a_0=0.12 nm is the graphene lattice constant[32]. The edge state becomes insulating when the edge is disordered, as it is the case for oxygen plasma etched free-standing graphene edges as stated in Refs. [29,45,46]. In contrast, the SiC substrate stabilizes epigraphene. This is dramatically demonstrated in epigraphene oxide that is produced by submersing epigraphene in a strongly oxidizing hot bath of potassium permanganate, sulfuric acid, and sodium nitrate. Yet, the epigraphene oxide layer that is formed is flat and reverts to pristine epigraphene when heated[47,48].

The chemistry of plasma etched epigraphene edges and the SiC surfaces involves C, Si, O, and H that are used in the processing. Here we use HF to remove surface oxides, that most likely

hydrogen terminates the edges. Moreover, post-processing thermal annealing may establish Si-C bonds at the edges (as in sidewall ribbons). The chemical bonding to the substrate is seen in cross sectional TEM studies of sidewall ribbons[14,49,50], showing that the SiC substrate chemically and mechanically stabilizes the graphene edges as well.

3. Non-polar Epigraphene Production and Characterization

The epigraphene laboratory in the Tianjin International Center for Nanoparticles and Nanostructures (TICNN) at the University of Tianjin, specifically established to develop epigraphene electronics, produced the non-polar SiC substrates and epigraphene, starting from commercial bulk single crystal 4H and 6H SiC stock. Figure 2 shows characterization of the epigraphene wafers produced using the confinement controlled sublimation method[51]. Upon heating epigraphene growth starts with trapezoidal islands (Fig. 2a) that subsequently merge, to produce a uniform flat graphene layer. Raman spectroscopy of the graphene indicates low defect graphene (Fig.2f).

Angle resolved photoelectron spectroscopy (ARPES) scans along the K-M-K' direction shows the K and K' Dirac cones with Dirac points at the Fermi level (Fig. 2d), revealing an isotropic carrier velocity $c^*= 1.04\ 10^6$ m/s at E=0, similar to sidewall graphene[14,52]. Scanning tunneling microscopy (Fig. 2b) shows graphene lattice, atomically resolved, and scanning tunneling spectroscopy (Fig. 2c) confirms that the graphene is neutral as are epigraphene sidewall ribbons ($|n_0|\leq 10^{10}$/cm^2 corresponding to a Fermi energy $E_F\leq$10 meV). In contrast, $E_F\approx$350 meV and $n\approx -10^{13}$/cm^2 in Si-face polar epigraphene.

In a magnetic field B, electrons in graphene organize in discrete energy Landau levels: $E(\nu) = \pm\sqrt{2|\nu|eB\hbar c^{*2}}$. Transitions from occupied to unoccupied Landau level are detected in infrared magneto-spectroscopy (Fig. 2e). The characteristic $\sqrt{B}$ dependence of the transitions is a signature of a graphene monolayer, from which $c^*=1.0\ 10^6$ m/s is determined, consistent with ARPES. This transition is observed at least down to B=0.25 T, indicating that $|n_0|$is at most $3.6\ 10^{10}$ cm^{-2}.

4. Segmentation of the edge state

Graphene Hall bars produced with standard nanoelectronics lithography methods were supplied with Pd-Au contacts (see Methods). The 30 nm thick Al_2O_3 dielectric used in the top gate is applied in high vacuum conditions as in previous epigraphene studies, including sidewall ribbons[14-16], high-mobility Hall bar structures[53] and ultra-high frequency field effect transistors[54].

Magneto-transport measurements were made at magnetic fields B ranging from -9 T to +9 T, temperatures T ranging from 2K to 300K, and charge densities n up to $4\ 10^{12}$cm^{-2}. The bulk charge density n is derived from the top gate potential $V_g=ne(1/C + 2/C_q)$, where C is the classical capacitance per unit area and $C_q= 2ne^2/E_F$ is the quantum capacitance[55,56], which we experimentally measured.

$V_{ij;kl}$ indicates the voltage difference between contacts k and l, with current injected between contacts i and j, hence $R_{ij;kl}= V_{kl}/I_{ij}$ and $G_{ij;kl}=1/R_{ij;kl}$. As usual, $V_{ij;kl}(B)$ is decomposed in its

symmetric and antisymmetric components: $V^X(B)=(V(B)+V(-B))/2$ (longitudinal voltage) and $V^Y(B)=(V(B)-V(-B))/2$ (Hall voltage), which also defines R^x and R^y.

Individual segment resistances R_i (see Fig. 1d for segment notation) were determined from the matrix of 2-point resistances of pairs of contacts measured at T=11 K, for n=0, n=6 10^{11} cm^{-2} and n=2.8 10^{12} cm^{-2}. Figure 3a shows that at CNP (n=0), $R_i=R_i^{edge}$ is about 40 kΩ. For $n\neq0$, $G_i^{bulk}=G_i(n)-G_i(CNP)$, following Eq.2. R_i^{bulk} increases linearly with segment length L_i and inversely with n. The mobility μ= 870 cm^{-2}V^{-1}s^{-1} corresponds to λ_{bulk} ≈10 nm (for $n=10^{12}$cm^{-2}). Hence we find that $R^{edge}(n=0,B=0,T=0)$=49±5 kΩ=1.9±0.2 R_0 where $R_0=h/e^2=1/G_0\approx25.8$ kΩ (the temperature dependence is extrapolated to T=0K, Fig. 3c inset). The mfp's of the segments at n=0 are then determined, using Eq. 2, as listed in the caption of Fig. 3.

Figure 3b plots the resistances for all measured values of $R^X_{15;kl}$ (n=0,B=9T, T=4.5, 40, 65K) versus the number of segments $N_{15;kl}$ from contact k to l, along the current path from contact 1 to contact 5 (Fig. 1d). It shows that $R^X_{15;kl}$ (n=0, B=9T,T)≈$N_{15;kl}$ R_0 (independent of T). A similar analysis for B=0, n=0 shows a linear dependence with $N_{15;kl}$ with temperature dependent slopes. The measured temperature dependence (Fig. 3c), that saturates below T=3K, allows conductances to be extrapolated to T=0K (Fig.3c inset). Hence we find that R^{edge} (B=9T,T) =0.98±0.03 R_0 and $R^{edge}(B=0T,T=0K)=R^{edge}$ (B=0T,T=2K)=2.08±0.27 R_0. We identify R^{edge} with R(n=0), see Eq. 1.

Figure (3d-e) shows conductance measurements of $G_1^{edge}=G^X_{15;12}$ (Segment 1) and $G_{15;15}$ (Segments 1,7,8, and 5 in series) at CNP. $G^X(n,B,T)$ increases linearly with B and saturates at G^X_{sat} for B_{sat}≈1.5T producing a "V" shape whose amplitude diminishes with increasing T. Similar saturation is found for increasing B and T. Also note that $G_{15;15}(n=0,B=9T,T)$ =0.255 G_0 (≈G_0/4 as expected for 4 segments), whereas $G_{15;12}(n=0,B=9T,T)$=0.78 G_0 (or 0.96 G_0 after adjusting for the measured mfp as described in Eq. 2).

For B=0, the T dependence (Fig.3c) is approximately described by $G(n,T)=(1+L_1/\lambda_1)^{-1}$ (G_0/2)(1+exp-T^*/T) + $G(n)$, with T^*≈12K, consistent with Eq. 2. The second term is the T independent diffusive (bulk) contribution. The first term is consistent with two 1D subbands, each with a conductance of ½ G_0 (not 1 G_0 as expected) and separated in energy by $\Delta E=k_BT^*$. Furthermore, the band shift ΔE decreases with increasing B, to produce the "V" shape of Fig. 3d-e suggesting a magnetic splitting[21,22]. Similar behavior was observed in Ref.[14] and cannot be explained by weak localization, that would imply a phase coherence length l_ϕ≈20 nm,[24] while in fact l_ϕ>1 μm as shown below.

Figures 4d,e,f show $G^X_{15;12}(n,T,B_i)$. $G^X_{15;12}(n,T$=4.5,40,65K,B_i<1T) increases linearly with increasing |n| with a sharp corner at n=0 (Fig. 4d, inset). The linear increase results from the parallel conductance contributions of the edge and the bulk as described in Eq. 2. This corner rounds somewhat at T=65K (Fig.4f, insert), due to thermal population of subbands at n=0. Since at T=65K, the thermal broadening exceeds the broadening due to charge disorder δn, we estimate that $(k_BT/\hbar c^*)^2 > \pi\delta n$, or δn<2.5 10^9/cm^2. Note that the conductance at n=0 at low temperatures, generically called the "residual conductance"[25], is here due to the edge state. It is not related to the minimum conductivity, that is due to charge disorder[25] ("charge puddles") that are essentially absent in epigraphene[57,58].

Hence, as described in Eq. 2, the EVE forms a network of ballistic segments, in parallel with a network of essentially T independent diffusive segments. However, in the quantum Hall regime (QHR), the bulk becomes insulating and transport is confined to the ballistic quantum Hall edge state that, then, is likely to interact with the EVE.

5. Quantum Hall Regime

Transport at larger magnetic fields, away from CNP, exhibits quantum Hall features, as shown in Fig 4a-f for $R^{Hall}=R_{15;26}$ and $R^{X}=R^{X}_{15;12}$. A single Hall plateau at $R^{Hall}=¼\ R_0$ (suggesting a bilayer) is observed while $R^{Hall}=½\ R_0$ is expected for the ν=0 Landau level of a monolayer. The absence of any evidence of second Landau level prevents immediate identification, but further analysis, below, supports a monolayer.

The EVE significantly affects the Hall effect. Symmetry requires that at E=0, the EVE current is half electron-like and half hole-like (Fig. 1c), so that its net Hall voltage vanishes[59] even though the net EVE current I^{edge} does not: a right moving electron carries the same current as a left moving hole so if both currents contribute equally, then no average Hall voltage is generated. Moreover, if these events are simultaneous (correlated) as suggested by its quantization, then the charge of the ribbon does not change in the process. (While resembling co-tunneling[60-63], co-tunneling is ruled out since the edge state conductance is quantized, and co-tunneling is not.)

As shown above, in the diffusive regime, the total current $I_0=I^{edge}+I^{bulk}=(G^{edge}+G^{bulk})V$ and G_{edge} is essentially independent of V_g. Therefore

$$G_{bulk}(n,B)=G(n,B)-G_{edge}(n,B)=G(n,B)-G(n=0,B) \quad \text{(a)}$$
$$I_{bulk}(n,B)=I_0\,(1-G^{X}(n=0,B)/G^{X}(n,B)) \quad \text{(b)}$$
$$R^{Y}_{bulk}(n,B)=R^{Y}(n,B)\ I_0/I_{bulk}. \quad \text{(c)} \qquad (4)$$

Equation 4 is expected to be relevant in the QHR and explains the anomalous quantum Hall resistance as summarized next.

(1) The EVE current affects the measured Hall plateau resistance, $R^{Y}(n,B)$ (Eq. 4c). Fig. 5a shows the corrected $R^{Y\,bulk}(n,B)\approx 0.4\ R_0$ which is close to the expected $R^{Hall}=½\ R_0$ for monolayer graphene.

(2) At fixed B_i and increasing n from n=0, $R^{Y}(n,B_i)$ initially follows a B_i-independent universal curve $R^{Uni}(n)$, characterized by non-quantized pseudo quantum Hall plateaus $R^{Y}(B,n_i)=R^{Uni}(n_i)$ as shown in Fig. 4g. We conclude that the pseudo-plateaus are in fact monolayer quantum Hall plateaus, however the shorting effect of the edge state reduces the quantized value by I^{bulk}/I_0, that vanishes at CNP and initially increases linearly with n as shown in Fig. 5b.

(3) Fig. 4a (dashed vertical lines) shows that the quantum Hall plateau is escaped for filling factor $F=(n_i/B_i)\phi_0\approx 4$, where $\phi_0=h/e$ is the flux quantum. Since this plateau extends to n=0, the mid-plateau filling factor is F=2, which corresponds to a monolayer (not a bilayer)[64].

(4) Normally, in the QHR, the quantum Hall edge states are protected ballistic conductors where backscattering is completely suppressed, and the 2-point resistance between any two

ohmic contacts is R^{Hall}. In contrast we observe $R^{X}_{15;15}$=1.6 R_0 instead of 0.25 R_0; $R^{X}_{15;12}$=0.6 R_0 instead of 0; $R^{X}_{15;23}$= 0.2 R_0 instead of 0; $R^{X}_{15;34}$=0.4 R_0 instead of 0 (lead resistances are <0.04 R_0). These observations are consistent with edge state backscattering at the junctions that is not suppressed, causing voltage drops at the junctions.

(5)The amplitude $A_{SdH}(B,T)$ of the $R^{X}(B,T)$ oscillations (Shubnikov-de Haas oscillations) are given by the Lifshitz-Kosevich equation: $A_{SdH}(B,T)/A_{SdH}(B,T=0K)=u/sinh(u)$, where $u=2\pi^2 k_B T/E_{LL}(B)$ and $E_{LL}(B)$ is the Landau level energy. For a monolayer it predicts[65]: $A_{SdH}(B=9T,T=150K)/A_{SdH}(B=9T,T=0K)=0.4$ and for a bilayer[66] $A_{SdH}(B=9T,T=150K)/A_{SdH}(B=9T,T=0K)=0.04$. In contrast, the observed amplitude is $A_{SdH}(B=9T,T=150K)/A_{SdH}(B=9T,T=0K)=0.25$. This is consistent with monolayer and not with a bilayer.

Hence we conclude that the anomalous Hall effect is caused by the EVE.

6. Coherence and non-local transport

Reproducible voltage fluctuations are observed at all contacts, for all magnetic fields and gate voltages. The fluctuations are Fabry-Perot interference patterns (FP) resulting from coherent scattering. For comparison, the FP of a gated carbon nanotube of length L consists of regular spaced oscillations with a period $\Delta k_F=\pi/L$ ($k_F=\sqrt{\pi n}$).[8] For multi-segment systems, the diffraction patterns are complex: the large number of paths from source to drain produces rich diffraction patterns.

The Hall resistance was measured in two configurations that are mutually rotated by 90°, i.e $R_{15;26}$ and $R_{26;15}$. $R_{15;26}(B_i)$ and $R_{26;15}(-B_i)$, that superimpose very well (Fig. 6a). These measurements were made 3 weeks apart, demonstrating the robustness of the diffraction pattern as also is clear from Figure 6b that overlaps $\Delta R_{15;26}$ (n,B_i) and $\Delta R_{26;15}(n,-B_i)$ for 27 values of B_i. In this Hall geometry, the measured fluctuations reflect voltage fluctuations at the junctions.

Figure 6c shows that the $R^{X}_{15;12}(n,B_i)$ and $R^{X}_{15;16}(n,B_i)$ are essentially identical. Classically, this result may be expected, since both configurations measure segment 1. However, they measure opposite edges, and fluctuations generated within opposite edges are not expected to be identical. This supports the picture that the fluctuations manifest in the junction region (i.e. they are not generated in the edges), even in the QHR.[67]

Figure 6d shows the Fourier spectrum of $R_{15;12}(k_F,B_i)$, that is plotted versus $(2\pi/k_F)^2=\lambda^2$ to bring out the striking quadratic dependence of the resonances: $\lambda^2_m=(\lambda_0(B_i)+m\Delta\lambda)^2$ where $\Delta\lambda$=0.67 μm independent of B, and $\lambda_0(B_i)/\Delta\lambda$ has a bimodal distribution peaked at ≈ ± 0.3. Note that the junction widths are 0.7 μm, corroborating the conclusion that the fluctuations are created at the junctions, and that tunneling is involved in the transport of the EVE at the junctions. These clearly important properties are not understood.

Coherent transport[68] is also indicated in the non-local voltage response from a remote current excitation as shown in Fig. 5c, d at several temperatures and magnetic fields. For B=9T and T=300K, the nonlocal resistance $R_{26;39}$ is about 1% of the local resistance $R_{39;39}$ while for diffusive transport, this ratio is $e^{-\pi L/W}=4\ 10^{-7}$. Nonlocal charge transport effects are frequently

observed in quantum Hall conductors[69], caused by non-equilibrated edge and bulk channels. Note the observed absence of T and n dependence for B=0, and the large non-local effect at B=9T that increases with increasing T and decreases with increasing n. These effects remain to be explained.

7. Future outlook

This work launches epigraphene electronics. It introduces the rich physics and the considerable applications potential of non-polar epigraphene.

Epigraphene is unique, providing crystallographically aligned graphene, with contamination-free interfaces, extremely low disorder[57,58] and mechanically and chemically stable edges[49]. It is produced on the wafer scale[70-72], compatible with current microelectronics fabrication processes while using relatively inexpensive single crystal electronics grade SiC substrates. This, combined with its extreme thermal, electrical, chemical and mechanical stability, makes epigraphene unique among the 2D materials: currently, only epigraphene qualifies as a potential low dimensional nanoelectronics platform.

Graphene's macromolecular nature[73] is reflected in its electronic properties, and introduces quantum coherence into electronics[22,74], which in turn is an essential feature of quantum computing. However, since the edge state is metallic, non-conventional switches based on quantum mechanical tunneling and quantum interference[3] need to be developed. Recently extraordinary, tunneling-like properties[75,76] have been demonstrated in sidewall ribbons provided with constrictions[75] and physical gaps[76] indicating that ultralow power tunnel field effect transistors[77] may be developed soon. Spin transport measurements[78] indicate spintronics[22] potential. Anticipating integration with silicon electronics, the GTEG already developed a wafer bonding technique to bond a ≈1 μm thick single crystal silicon sheet on top of the patterned epigraphene layer[79].

But, first, fundamental scientific questions need to be resolved[11,33]. For example, why is the edge state mean free path 1000 times greater than the bulk even though the edges are by no means perfect? What is the nature of the two states and the symmetry breaking that produces the energy gap? Why is the conductance half of what is expected[12,80]? What causes the unusual resonance spectrum of the edge state? Moreover, since edge state transport is pinned to the Dirac point, and topologically non-trivial, could there be a connection with Majorana fermions[81-84]?

Regardless of the answers to these questions, it is already clear that non-polar epigraphene is an important new platform both for fundamental physics and for future electronics.

Corresponding authors
e-mail: walter.deheer@physics.gatech.edu
e-mail: maleixinjiang@tju.edu.cn

Acknowledgements

Financial support is acknowledged from the National Natural Science Foundation of China (No 11774255), the Key Project of Natural Science Foundation of Tianjin City (No 17JCZDJC30100), and the Double First-Class Initiative of Tianjin University from the Department of Education in China. Financial support was provided by the U.S. Air Force Office of Scientific Research under grant No FA9550-13-0217 and by the U. S. National Science Foundation-Division of Electrical, Communications and Cyber Systems (No 1506006) and NSF-Division of Material Research No 1308835. C.B, and V.P acknowledge funding from the European Union grant agreements No. 696656 and No 785219. This work was also made possible by the French American Cultural Exchange council through a Partner University Fund project. The magneto-infrared spectroscopy measurement was supported by the U.S. Department of Energy (grant No. DE-FG02-07ER46451) and performed at the National High Magnetic Field Laboratory, which is supported by NSF Cooperative Agreement No. DMR-1644779 and the State of Florida.
We thank David Wander for technical assistance with STS, Evangelos Papalazarou as well as François Bertrand and Patrick Lefebvre (local contacts) for their help with the ARPES measurement at the synchrotron Soleil- Cassiopée beam line, where the ARPES experiment was performed. WdH thanks P.N. First, A. Tzalenchuk and G. Mele for helpful conversations.

References

1 Berger, C., Conrad, E. & de Heer, W. A. in *Physics of Solid Surfaces, Landolt Börstein encyclopedia* Vol. Subvolume B *Physics of Solid Surfaces* (ed P. Chiaradia G. Chiarotti) Ch. 164-171, 727-807. ArXv:1704.00374 (Springer-Verlag, 2018).

2 Van Bommel, A. J., Crobeen, J. E. & Van Tooren, A. LEED and Auger electron observations of the SiC(0001) surface. *Surface Science* **48**, 463-472 (1975).

3 de Heer, W. A., Berger, C. & First, P. N. Patterned thin films graphite devices and methods for making the same. US patent (Filed June 12 2003 US patent 7015142, (provisional Application No.60/477,997 filed June 12 2003, Issued March 21 2006). EP patent 1636829B1 (issued Nov 23, 2016).).

4 Frank, S., Poncharal, P., Wang, Z. L. & de Heer, W. A. Carbon nanotube quantum resistors. *Science* **280**, 1744-1746 (1998).

5 Fujita, M., Wakabayashi, K., Nakada, K. & Kusakabe, K. Peculiar localized state at zigzag graphite edge. *J Phys Soc Jpn* **65**, 1920-1923 (1996).

6 Nakada, K., Fujita, M., Dresselhaus, G. & Dresselhaus, M. S. Edge state in graphene ribbons: Nanometer size effect and edge shape dependence. *Physical Review B* **54**, 17954-17961 (1996).

7 Bliss, D. F. *et al.* in *Single Crystals of Electronic Materials* (ed Roberto Fornari) (Woodhead Publishing, 2019).

8 Liang, W. J. *et al.* Fabry-Perot interference in a nanotube electron waveguide. *Nature* **411**, 665-669 (2001).

9 Bachtold, A., Hadley, P., Nakanishi, T. & Dekker, C. Logic circuits with carbon nanotube transistors. *Science* **294**, 1317-1320 (2001).

10 Ando, T. & Suzuura, H. Presence of perfectly conducting channel in metallic carbon nanotubes. *J Phys Soc Jpn* **71**, 2753-2760 (2002).
11 Lado, J. L., Garcia-Martinez, N. & Fernandez-Rossier, J. Edge states in graphene-like systems. *Synthetic Met* **210**, 56-67 (2015).
12 Allen, M. T. *et al.* Spatially resolved edge currents and guided-wave electronic states in graphene. *Nature Physics* **12**, 128-133 (2016).
13 Sprinkle, M. *et al.* Scalable templated growth of graphene nanoribbons on SiC. *Nat Nanotechnol* **5**, 727-731 (2010).
14 Baringhaus, J. *et al.* Exceptional ballistic transport in epitaxial graphene nanoribbons. *Nature* **506**, 349-354 (2014).
15 Ruan, M. *et al.* Epitaxial graphene on silicon carbide: Introduction to structured graphene. *MRS Bulletin* **37**, 1138-1147 (2012).
16 Ruan, M. *Structured epitaxial graphene for electronics* PhD thesis, PhD - Georgia Institute of Technology, (2012).
17 Laird, E. A. *et al.* Quantum transport in carbon nanotubes. *Rev Mod Phys* **87**, 703-764 (2015).
18 Wakabayashi, K., Takane, Y., Yamamoto, M. & Sigrist, M. Edge effect on electronic transport properties of graphene nanoribbons and presence of perfectly conducting channel. *Carbon* **47**, 124-137 (2009).
19 Castro Neto, A. H., Guinea, F., Peres, N. M. R., Novoselov, K. S. & Geim, A. K. The electronic properties of graphene. *Rev Mod Phys* **81**, 109-162 (2009).
20 Akhmerov, A. R. & Beenakker, C. W. J. Boundary conditions for Dirac fermions on a terminated honeycomb lattice. *Physical Review B* **77**, 085423 (2008).
21 Abanin, D. A., Lee, P. A. & Levitov, L. S. Spin-filtered edge states and quantum hall effect in graphene. *Physical Review Letters* **96** (2006).
22 Slota, M. *et al.* Magnetic edge states and coherent manipulation of graphene nanoribbons. *Nature* **557**, 691-+ (2018).
23 Kane, C. L. & Mele, E. J. Quantum spin Hall effect in graphene. *Physical Review Letters* **95**, 226801 (2005).
24 Datta, S. *Electronic transport in mesoscopic systems*. (Cambridge University Press, 1995).
25 Chen, J. H. *et al.* Charged-impurity scattering in graphene. *Nature Physics* **4**, 377-381 (2008).
26 Nomura, K. & MacDonald, A. H. Quantum transport of massless dirac fermions. *Physical Review Letters* **98**, 256602 (2007).
27 Aprojanz, J. *et al.* Ballistic tracks in graphene nanoribbons. *Nat Commun* **9** (2018).
28 Han, M. Y., Brant, J. C. & Kim, P. Electron Transport in Disordered Graphene Nanoribbons. *Physical Review Letters* **104**, 056801 (2010).
29 Young, A. F. *et al.* Tunable symmetry breaking and helical edge transport in a graphene quantum spin Hall state. *Nature* **505**, 528-532 (2014).
30 Mayorov, A. S. *et al.* Micrometer-Scale Ballistic Transport in Encapsulated Graphene at Room Temperature. *Nano Lett* **11**, 2396-2399 (2011).
31 Das Sarma, S., Adam, S., Hwang, E. H. & Rossi, E. Electronic transport in two-dimensional graphene. *Review of modern physics* **83**, 407-466 (2011).
32 Guo, J., Yoon, Y. & Ouyang, Y. Gate Electrostatics and Quantum Capacitance of Graphene Nanoribbons. *Nano Lett* **7**, 1935-1940 (2007).

33 Jackiw, R. & Rebbi, C. Solitons with Fermion Number 1/2. *Phys Rev D* **13**, 3398-3409 (1976).
34 Plasser, F. *et al.* The Multiradical Character of One- and Two-Dimensional Graphene Nanoribbons. *Angew Chem Int Edit* **52**, 2581-2584 (2013).
35 Stein, S. E. & Brown, R. L. Pi-Electron Properties of Large Condensed Polyaromatic Hydrocarbons. *J Am Chem Soc* **109**, 3721-3729 (1987).
36 Sun, Z. & Wu, J. S. Open-shell polycyclic aromatic hydrocarbons. *J Mater Chem* **22**, 4151-4160 (2012).
37 Zheng, P. *et al.* Hydrogenation of Graphene Nanoribbon Edges: Improvement in Carrier Transport. *IEEE Electr Dev Let* **34**, 707-709 (2013).
38 Brenner, K., Yang, Y. X. & Murali, R. Edge doping of graphene sheets. *Carbon* **50**, 637-645 (2012).
39 Tao, C. G. *et al.* Spatially resolving edge states of chiral graphene nanoribbons. *Nature Physics* **7**, 616-620 (2011).
40 Kobayashi, Y., Fukui, K., Enoki, T. & Kusakabe, K. Edge state on hydrogen-terminated graphite edges investigated by scanning tunneling microscopy. *Physical Review B* **73**, 125415 (2006).
41 Baringhaus, J., Edler, F. & Tegenkamp, C. Edge-states in graphene nanoribbons: a combined spectroscopy and transport study. *Journal of Physics-Condensed Matter* **25** (2013).
42 Deng, H. Y. & Wakabayashi, K. Vacancy effects on electronic and transport properties of graphene nanoribbons. *Physical Review B* **91**, 035425 (2015).
43 Massabeau, S. *et al.* Evidence of Fermi level pinning at the Dirac point in epitaxial multilayer graphene. *Physical Review B* **95**, 085311 (2017).
44 Janssen, T. J. B. M. *et al.* Anomalously strong pinning of the filling factor $\nu = 2$ in epitaxial graphene. *Physical Review B* **83**, 233402 (2011).
45 Tan, Y. W. *et al.* Measurement of scattering rate and minimum conductivity in graphene. *Physical Review Letters* **99**, 246803 (2007).
46 Yan, J. & Fuhrer, M. S. Charge Transport in Dual Gated Bilayer Graphene with Corbino Geometry. *Nano Lett* **10**, 4521-4525 (2010).
47 Wei, Z. Q. *et al.* Nanoscale Tunable Reduction of Graphene Oxide for Graphene Electronics. *Science* **328**, 1373-1376 (2010).
48 Wu, X. *et al.* Epitaxial-graphene/graphene-oxide junction: An essential step towards epitaxial graphene electronics. *Physical Review Letters* **101**, 026801 (2008).
49 Palacio, I. *et al.* Atomic Structure of Epitaxial Graphene Sidewall Nanoribbons: Flat Graphene, Miniribbons, and the Confinement Gap. *Nano Lett* **15**, 182−189 (2015).
50 Norimatsu, W. & Kusunoki, M. Formation process of graphene on SiC (0001). *Physica E* **42**, 691-694 (2010).
51 de Heer, W. A. *et al.* Large area and structured epitaxial graphene produced by confinement controlled sublimation of silicon carbide. *Proc Nat Acad Sci* **108**, 16900-16905 (2011).
52 Hicks, J. *et al.* A wide-bandgap metal-semiconductor-metal nanostructure made entirely from graphene. *Nature Physics* **9**, 49-54 (2013).
53 Hu, Y. *et al.* Structured epitaxial graphene: growth and properties. *Journal of Physics D-Applied Physics* **45**, 154010 (2012).

54 Guo, Z. L. *et al.* Record Maximum Oscillation Frequency in C-Face Epitaxial Graphene Transistors. *Nano Lett* **13**, 942-947 (2013).
55 Das, A. *et al.* Monitoring dopants by Raman scattering in an electrochemically top-gated graphene transistor. *Nat Nanotechnol* **3**, 210-215 (2008).
56 Fang, T., Konar, A., Xing, H. L. & Jena, D. Carrier statistics and quantum capacitance of graphene sheets and ribbons. *Appl Phys Lett* **91**, 092109 (2007).
57 Nachawaty, A. *et al.* Magnetic field driven ambipolar quantum Hall effect in epitaxial graphene close to the charge neutrality point. *Physical Review B* **96**, 075442 (2017).
58 Curtin, A. E. *et al.* Kelvin probe microscopy and electronic transport in graphene on SiC(0001) in the minimum conductivity regime. *Appl Phys Lett* **98**, 243111 (2011).
59 Ashcroft, N. W. & Mermin, N. D. Solid State Physics. *HRW International Editions* (1988).
60 Liang, W. J., Bockrath, M. & Park, H. Shell filling and exchange coupling in metallic single-walled carbon nanotubes. *Physical Review Letters* **88**, 126801 (2002).
61 Sigrist, M. *et al.* Phase coherence in the inelastic cotunneling regime. *Physical Review Letters* **96**, 036804 (2006).
62 Gao, B., Glattli, D. C., Placais, B. & Bachtold, A. Cotunneling and one-dimensional localization in individual disordered single-wall carbon nanotubes: Temperature dependence of the intrinsic resistance. *Physical Review B* **74**, 085410 (2006).
63 Nygard, J., Cobden, D. H. & Lindelof, P. E. Kondo physics in carbon nanotubes. *Nature* **408**, 342-346 (2000).
64 Alexander-Webber, J. A. *et al.* Giant quantum Hall plateaus generated by charge transfer in epitaxial graphene. *Sci Rep-Uk* **6**, 30296 (2016).
65 Küppersbusch, C. & Fritz, L. Modifications of the Lifshitz-Kosevich formula in two-dimensional Dirac systems. *Physical Review B* **96**, 205410 (2017).
66 Castro, E. V. *et al.* Biased bilayer graphene: Semiconductor with a gap tunable by the electric field effect. *Physical Review Letters* **99**, 216802 (2007).
67 Martins, F. *et al.* Coherent tunnelling across a quantum point contact in the quantum Hall regime. *Sci Rep-Uk* **3**, 1416 (2013).
68 Berger, C. *et al.* Electronic confinement and coherence in patterned epitaxial graphene. *Science* **312**, 1191-1196 (2006).
69 Abanin, D. A. *et al.* Giant Nonlocality Near the Dirac Point in Graphene. *Science* **332**, 328-330 (2011).
70 Emtsev, K. V. *et al.* Towards wafer-size graphene layers by atmospheric pressure graphitization of silicon carbide. *Nature Materials* **8**, 203-207 (2009).
71 Robinson, J. *et al.* Nucleation of Epitaxial Graphene on SiC(0001). *Acs Nano* **4**, 153-158 (2010).
72 Kruskopf, M. & Elmquist, R. E. Epitaxial graphene for quantum resistance metrology. *Metrologia* **55**, R27-R36 (2018).
73 Boehm, H. P., Setton, R. & Stumpp, E. Nomenclature and Terminology of Graphite-Intercalation Compounds (Iupac Recommendations 1994). *Pure Appl Chem* **66**, 1893-1901 (1994).
74 Baer, R. & Neuhauser, D. Phase coherent electronics: A molecular switch based on quantum interference. *J Am Chem Soc* **124**, 4200-4201 (2002).
75 Baringhaus, J. *et al.* Electron Interference in Ballistic Graphene Nanoconstrictions. *Physical Review Letters* **116**, 186602 (2016).

76 Palmer, J. *Pre-growth structures for nanoelectronics of EG on SiC* PhD thesis, Georgia Inst. Techn, (2014).
77 Katkov, V. L. & Osipov, V. A. Review Article: Tunneling-based graphene electronics: Methods and examples. *J Vac Sci Technol B* **35**, 04E101 (2017).
78 Hankinson, J. *Spin dependent current injection into epitaxial graphene nanoribbons* PhD thesis, PhD - Georgia Institute of Technology, (2015).
79 Dong, R. *et al.* Wafer bonding solution to epitaxial graphene-silicon integration. *Journal of Physics D-Applied Physics* **47**, 094001 (2014).
80 Ji, W. J. & Wen, X. G. 1/2 (e(2)/h) Conductance Plateau without 1D Chiral Majorana Fermions. *Physical Review Letters* **120**, 107002 (2018).
81 He, Q. L. *et al.* Chiral Majorana fermion modes in a quantum anomalous Hall insulator–superconductor structure. *Science* **357**, 294-299 (2017).
82 Groning, O. *et al.* Engineering of robust topological quantum phases in graphene nanoribbons. *Nature* **560**, 209-+ (2018).
83 San-Jose, P., Lado, J. L., Aguado, R., Guinea, F. & Fernandez-Rossier, J. Majorana Zero Modes in Graphene. *Physical Review X* **5**, 041042 (2015).
84 Lian, B., Sun, X. Q., Vaezi, A., Qi, X. L. & Zhang, S. C. Topological quantum computation based on chiral Majorana fermions. *P Natl Acad Sci USA* **115**, 10938-10942 (2018).

Figure Captions

Fig.1 *The epigraphene edge state*. **(a)** Schematic diagram of a top gated epigraphene edge (to scale). Electric fields **E** for a negative gate voltage V_g are represented as black arrows. **(b)** The charge density $n(x)$ that is induced on the graphene by the gate voltage V_g is depleted near the edge and absorbed in the empty states of the flat band at the edge, thereby pinning the Fermi level to E=0 at the edge. Moving away from the edge, the Dirac point energy E_D sinks below the Fermi level. Far from the edge $eV_g=dn_0+hc*k_F$ where $k_F=\sqrt{\pi n}$ and d is the dielectric thickness. Note that the Fermi wavelength λ_F diverges at the edge and converges to its bulk value $2\pi/k_F$ far from the edge. **(c)** One valley of the graphene ribbon band structure for a 700 nm wide ribbon, showing the edge state, composed of a flat band localized at the edge (FB), two linear delocalized dispersing bands (LB+ and LB-), and the hyperbolic bulk 1D subbands (bulk bands). Near E=0 the edge state is evanescent (EVE) and decays in the bulk. Only the EVE participates in the transport for E=0. **(d)** Schematic diagram of the top gated Hall bar consisting of 8 contacts, 10 segments (branches of the crosses) and 3 junctions (central region of the 3 crosses). Numbers correspond to contacts and their associated segments. Segments 7 and 8 are internal. The segment lengths measured in μm from contact to junction, are L_1=3.57; L_2=1.56; L_3=4.00; L_4=3.26; L_5=4.5; L_6=3.64; L_7=3.28; L_8=1.69 μm. Segment widths are 700 nm.

Fig.2 *Non-polar epigraphene characterization*. **(a)** *SEM* micrograph of trapezoidal graphene islands that form early in the growth and ultimately coalesce to produce a uniform graphene layer. **(b)** *Low temperature STM* image of the epigraphene. The inset shows the characteristic hexagonal lattice of graphene. **(c)** *STS.* Typical scanning tunneling spectrum obtained at 4.4K (I_{set}=400 pA at V_{bias}=500 mV) , showing the characteristic graphene density of states. A linear fit (dashed lines) indicates a doping level E_F-E_D<6 meV, showing that the graphene is essentially charge neutral. **(d)** *ARPES* (197.45 eV) taken along K-M-K' showing characteristic graphene Dirac cones with c^*=1.06 10^8cm/s, that terminate at E=0 confirming charge neutrality and no significant anisotropy. **(e)** *Infrared magneto-spectroscopy.* The transitions following the expected characteristic graphene $\sqrt{B}$ dispersion (indicated by the red lines) confirming its monolayer character. **(f)** *Raman spectroscopy*. Raw spectrum (red) and SiC subtracted spectrum (blue). The 2D peak position and width are typical of a graphene monolayer. The G peak and D are somewhat distorted, probably due to the buffer-layer like interface layer.

Fig.3 *Segmentation*. **(a)** Segment resistances $R_i(B=0,n)$ versus segment length L_i at T=11K and B=0, extracted from a matrix of 2 point measurements, showing that $G_i(n)=G_i(n=0)+ne\mu W/L_i = G_i^{edge} + G_i^{bulk}$; ($G_i=1/R_i$). $R^{edge}(L_i,B=0,n=0)$, (blue dots); $R^{bulk}(L_i,B=0, n=6\ 10^{11}cm^{-2})$, (red dots); and $R^{bulk}(L_i,B=0,n=2.8\ 10^{12}cm^{-2})$, (green dots), corresponding to μ=870 $cm^2V^{-1}s^{-1}$. Extrapolating to T=0 (Fig. 3c inset), with λ_l=19 μm (see below), then (Eq.2) $1/g_0=R^{edge}(B=0,n=0,T=0K)/(1+L_1/\lambda_1)\approx 2\ R_0$, where $R_0=h/e^2$ (black dots). **(b)** $R_{15;ij}$ at n=0 at T=4.5K (blue), 40K (green) and 65K (red) versus N_{seg}, the number of segments along the current path (1-5) from i to j. For B=9T (triangles: data, solid color lines: linear fit), the excited state resistance $R_{ex}^{edge}/N_{seg}=0.98\pm0.03\ R_0$, independent of T. Extrapolating the B=0T data (Circles: data, dashed lines: linear fit) to T=0 (Fig. 3c inset), yields the ground state resistance at T=0: $R_{gr}^{edge}/N_{seg}=2.08\pm0.27\ R_0$ (stars: data, black line: linear fit) **(c)** Temperature dependence $G^{edge}(T,B=0,n=0)$ showing saturation at $G_0/2$ for T=0K (inset) and an asymptotic approach to $G=1\ G_0$ for large T. Measurements of $G^X_{15;12}(T,B=0,n)$ for n=7 10^{11} cm^{-2} (blue), n=2 10^{12} cm^{-2}

(green), and n=4 10^{12} cm^{-2} (red) that are rigidly shifted to coincide with $G^X_1(T$=4.5K,B=0,n=0) show good mutual overlap for all T, consistent with Eq. 2. Also shown is $G^{edge}(T,B$=9T,n=0) (black diamonds) that is substantially temperature independent. **(d)** $G^X_{15;12}(n$=0,B,T) for T=4.5K (blue); 40K (green); 65K (red) showing "V" shape behavior, extending from G≈1/2 G_0 to G≈1 G_0 **(d)** $G^X_{15;15}(n$=0,B,T) for T=4.5K (blue); 40K (green); 65K (red) showing "V" shape that is approximately ¼ of $G^X_{15;12}(n$=0,B,T) as expected for 4 segments in series. These measurements are consistent with the high temperature and/or large magnetic field single segment resistance R^{edge}=1 R_0 as found in Ref.14. The edge state segment mfp's compiled from all measurements of all segments are: λ_1=19 μm; λ_2>40 μm; λ_3=26 μm; λ_5=34 μm; λ_6>40 μm; λ_7=17 μm; λ_9>40 μm.

Fig.4. *Magneto-transport*. Hall resistance ($R^{Hall}=R_{15;26}$) and longitudinal conductance ($G^X_{15;12}$, top edge and $G^X_{15;16}$, bottom edge) for T= 4.5K **(a,d)**; T=40K **(b,e)**; T=65K **(c,f)** and B=±[9 …1 ,0.5, 0.25, 0]T. Positive B gives positive Hall and corresponding colors identifies $G^X_{15;12}$. Negative B gives negative Hall and corresponding color identifies $G^X_{15;16.}$ Note that $G^X_{15;12}$ and $G^X_{15;16}$ overlap well. Note that for B≤1T, $G^X(n,B,T)=G^X(n$=0,$B,T)+n$C, where C=5.3 10^{-13} G_0.cm^2 and $G^X(n$=0,B,T) follows "V" (Fig.3.d), showing that the edge state and bulk state are in parallel, as described in Eq. 2. The sharp corner in G^X at n=0, T=4.5K rounds for T=65K, consistent with $\delta n<2.5\ 10^9$ cm^{-2}. Note also the quantum Hall plateau at $R^{Hall}=\pm 0.25R_0$ (a,b,c) and the $R_{15;26}(B_i,n)$ that all converge to a universal envelope curve merging into the Hall plateau $R^{uni}(n)$. The various $R^{Hall}(B_i,n)$ escape from the $R^{uni}(n)$ for B_i=0.9n_i T (n_i in 10^{12}cm^{-2}), consistent with a monolayer (see text). This indicates that the entire universal curve is the |ν|=2 Hall plateau, which is not constant, because of the "shorting" effect of the edge state. This causes the non-quantized pseudo-plateaus $R^{Hall}(n_i,B)$ presented in **(g)**. **(h)** Empirical determination of the quantum capacitance (QC) from $B/R^{Hall}(n,B_i)$; B_i=1T(red)-9T(blue) and 0.5T(black). Light lines, without QC so that n is proportional with V_g; bold lines, with QC correction (see text for details).

Fig.5. (a) Renormalized Hall plateaus for indicated B_i, assuming edge state conductance does not depend on n, and that the edge state current does not produce a Hall voltage. **(b)** Corresponding renormalized Hall currents, which increase from I_{Hall}/I_0=0 for n=0, to I_{Hall}/I_0=0.5 for large n and B. **(c)** Demonstration of non-local transport: $R_{local}=R_{26;26;}(n,B,T)$; $R_{nonlocal}=R_{26;39;}(n,B,T)$. $R_{nonlocal}/R_{local}$ or various T and B (see legend). Classically from the geometry $R_{26;39}/R_{39;39}$ is expected to be 10^{-7} and independent of n, B, and T.

Fig.6. *Fluctuations at T=4.5K*. **(a)** $R_{15;26}(n,B_i)$ compared with $R_{26;15}(n,-B_i)$. Note the remarkable overlap, considering the different configurations and different times of the measurements, which indicates that robust fluctuations are generated at the junction, even in the QHR. Note the sign changes. **(b)** Same as (a), after subtraction of smooth background and vertical shift. Note the weak B dependence. **(c)** Fluctuations in R^X: $\Delta R_{15;12}(n,B_i)$ (top edge of Segment 1) compared with $\Delta R_{15;16}(n,B_i)$ (bottom edge of Segment 1), showing essentially identical fluctuations, indicating shorting at the junction due to the edge state. **(d)** Logarithm of the amplitude of the Fourier transform of $R_{15;12}(B_i,k_F)$ ($k_F=\sqrt{\pi n}$) showing significant structure, indicating coherent quantum interference from micron scale structures in the Hall bar (analogous to Fabry-Perot interference). The spectra are shifted vertically, and the B_i (in Tesla) are indicated at the right border.

Figure 1

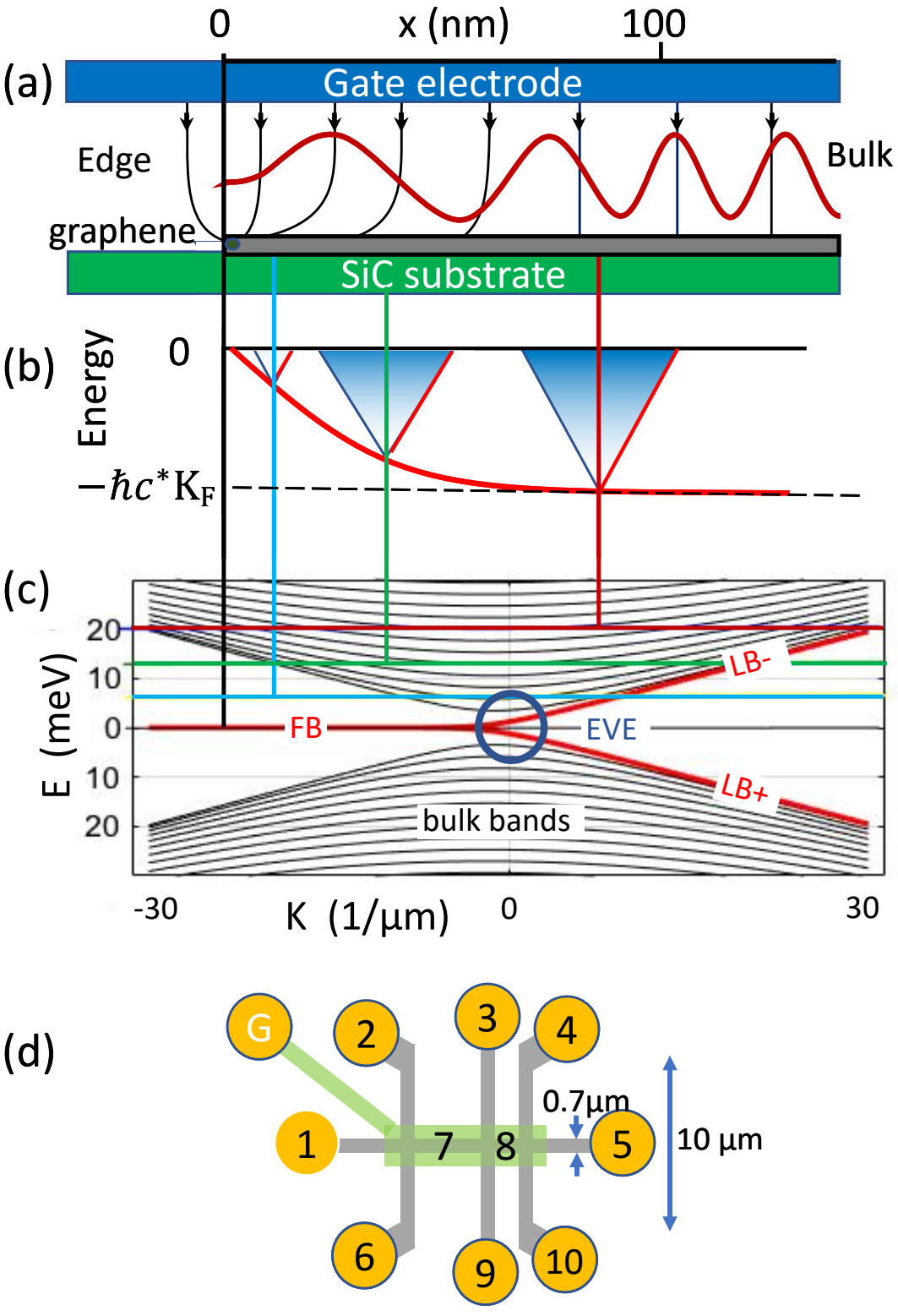
0
x (nm)
100
(a)
Gate electrode
Edge
Bulk
graphene
SiC substrate
(b)
Energy
0
$-\hbar c^* K_F$
(c)
20
10
0
10
20
E (meV)
LB-
FB
EVE
LB+
bulk bands
-30
K (1/μm)
0
30
(d)
G
2
3
4
1
7
8
5
6
9
10
0.7μm
10 μm

Figure 2

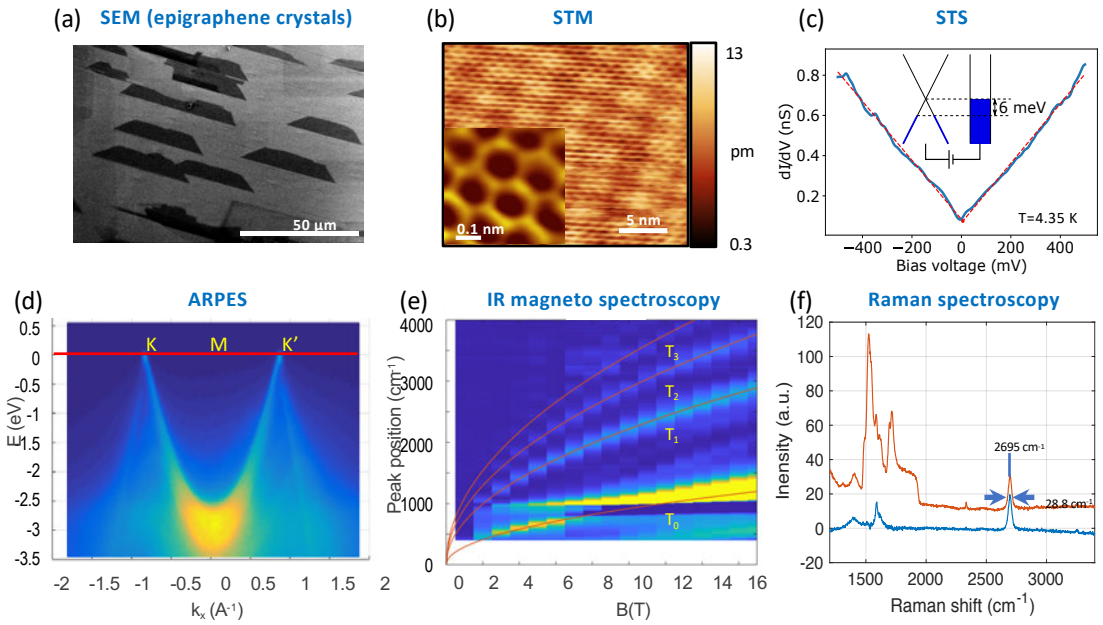
(a) SEM (epigraphene crystals)
50 μm
(b) STM
13
pm
0.3
0.1 nm
5 nm
(c) STS
dI/dV (nS)
Bias voltage (mV)
T=4.35 K
(d) ARPES
K
M
K′
E (eV)
k_x (A^{-1})
(e) IR magneto spectroscopy
Peak position (cm^{-1})
B(T)
T_3
T_2
T_1
T_0
(f) Raman spectroscopy
Inensity (a.u.)
2695 cm^{-1}
28.8 cm^{-1}
Raman shift (cm^{-1})

Figure 3

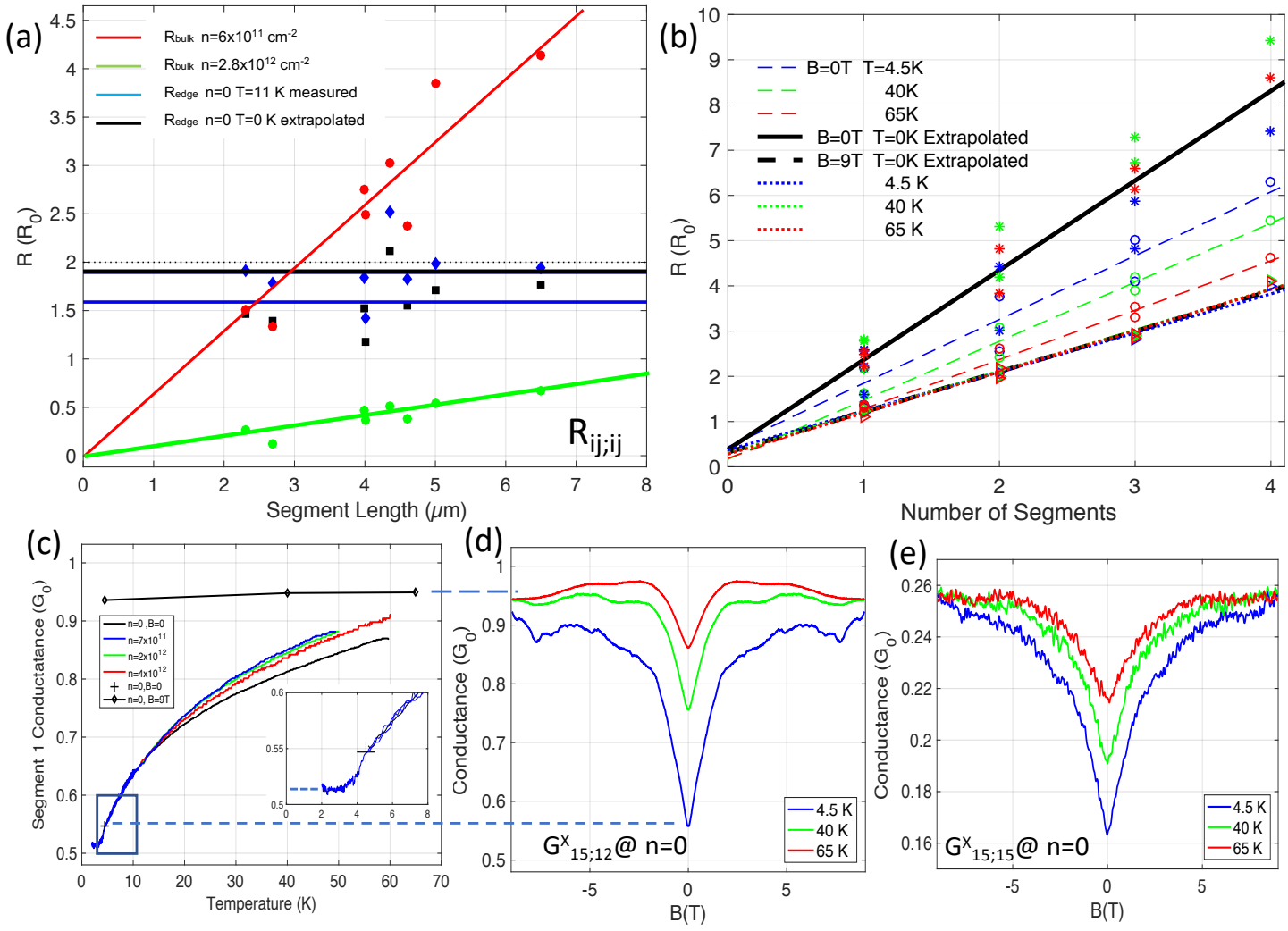
(a)
Rbulk n=6x10^11 cm^-2
Rbulk n=2.8x10^12 cm^-2
Redge n=0 T=11 K measured
Redge n=0 T=0 K extrapolated
R (R0)
Segment Length (μm)
Rij;ij
(b)
B=0T T=4.5K
40K
65K
B=0T T=0K Extrapolated
B=9T T=0K Extrapolated
4.5 K
40 K
65 K
R (R0)
Number of Segments
(c)
Segment 1 Conductatance (G0)
n=0 ,B=0
n=7x10^11
n=2x10^12
n=4x10^12
n=0,B=0
n=0, B=9T
Temperature (K)
(d)
Conductance (G0)
4.5 K
40 K
65 K
G^X 15;12@ n=0
B(T)
(e)
Conductance (G0)
4.5 K
40 K
65 K
G^X 15;15@ n=0
B(T)

Figure 4

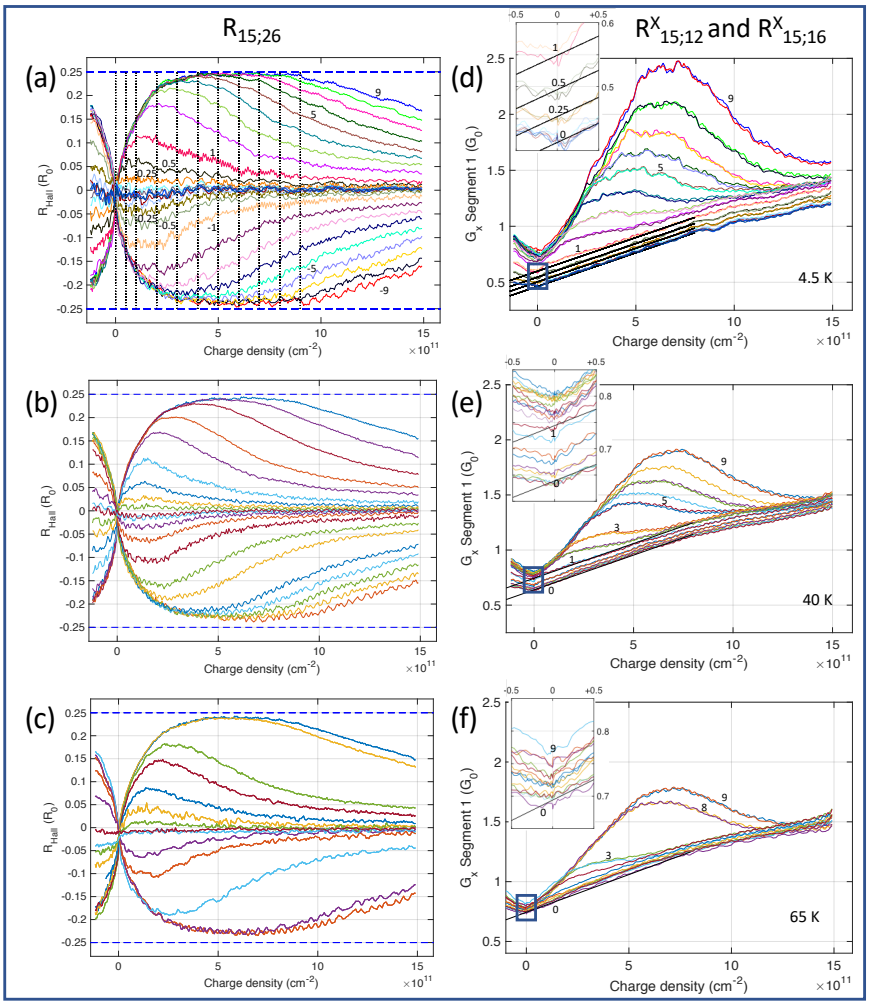
R15;26
R^X15;12 and R^X15;16
(a)
(b)
(c)
(d)
(e)
(f)
R_Hall (R_0)
G_x Segment 1 (G_0)
Charge density (cm^-2)
×10^11
4.5 K
40 K
65 K

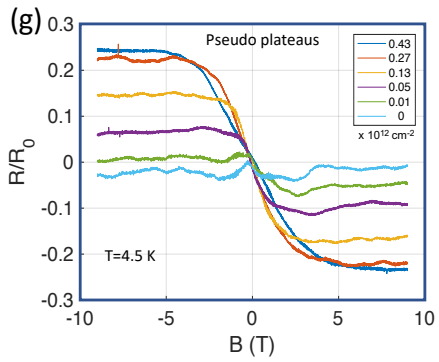
(g)
Pseudo plateaus
0.43
0.27
0.13
0.05
0.01
0
x 10^12 cm^-2
T=4.5 K
R/R_0
B (T)

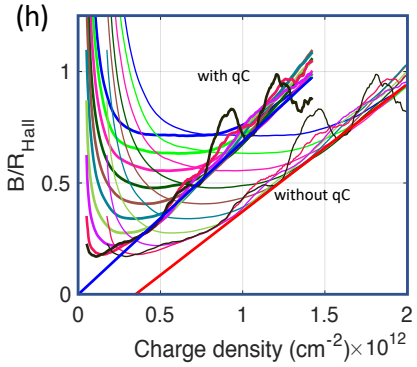
(h)
with qC
without qC
B/R_Hall
Charge density (cm^-2)×10^12

Figure 5

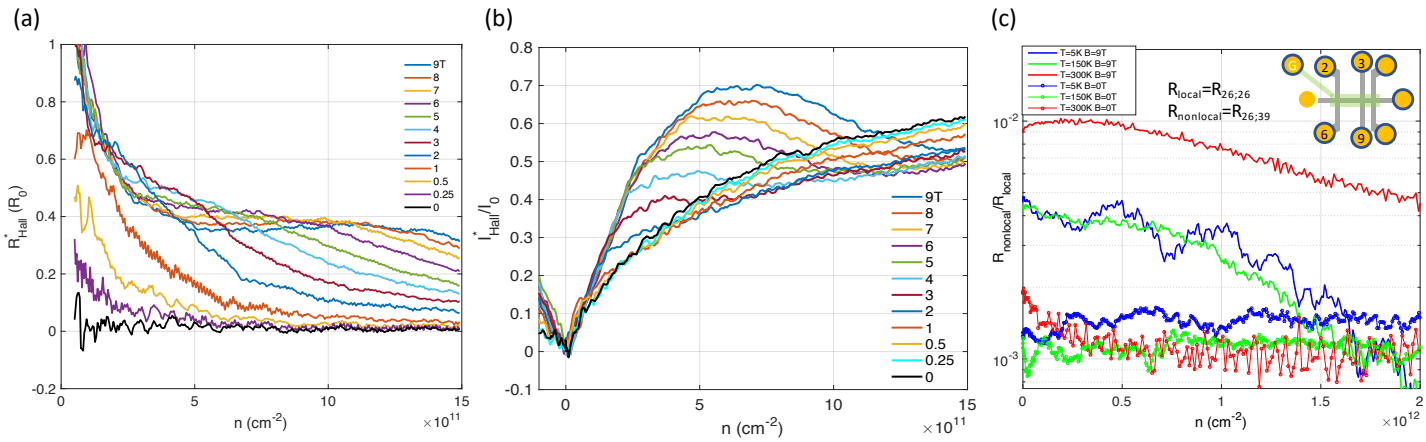
(a)
(b)
(c)
9T
8
7
6
5
4
3
2
1
0.5
0.25
0
n (cm-2)
×10^11
×10^12
T=5K B=9T
T=150K B=9T
T=300K B=9T
T=5K B=0T
T=150K B=0T
T=300K B=0T
Rlocal=R26;26
Rnonlocal=R26;39

Figure 6

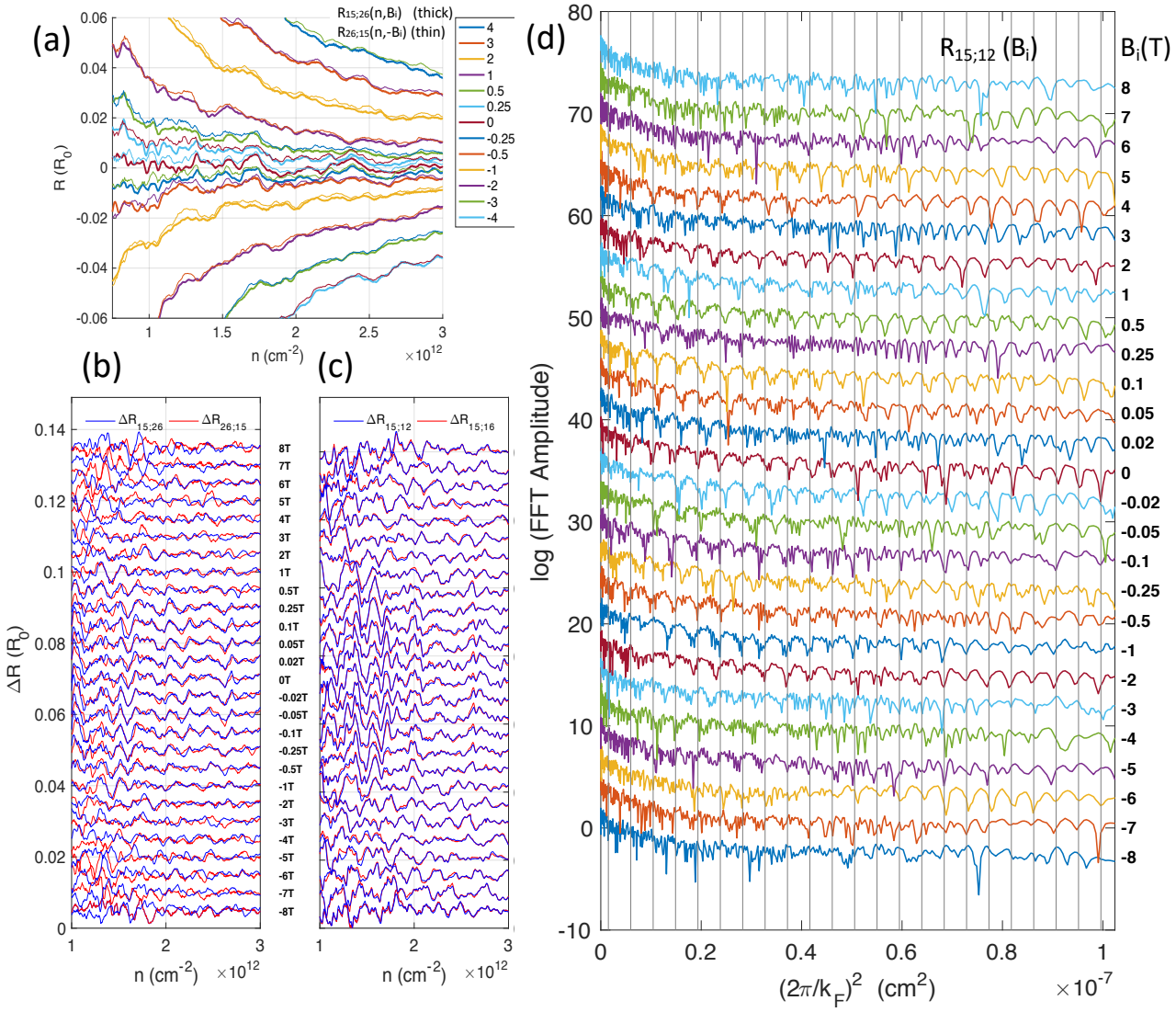
(a)
R15;26(n,Bi) (thick)
R26;15(n,-Bi) (thin)
R (R0)
n (cm-2)
×10^12
(b)
ΔR15;26
ΔR26;15
ΔR (R0)
n (cm-2)
×10^12
(c)
ΔR15;12
ΔR15;16
n (cm-2)
×10^12
(d)
R15;12 (Bi)
Bi(T)
log (FFT Amplitude)
(2π/kF)2 (cm2)
×10^-7